



BNL-223500-2022-JAAM

Noisy-Intermediate-Scale Quantum Electromagnetic Transients Program

Y. Zhou, P. Zhang

To be published in "IEEE Transactions"

August 2022

Interdisciplinary Science Department
Brookhaven National Laboratory

U.S. Department of Energy

USDOE Office of Electricity Delivery and Energy Reliability (OE), Power Systems Engineering
Research and Development (OE-10)

Notice: This manuscript has been authored by employees of Brookhaven Science Associates, LLC under Contract No. DE-SC0012704 with the U.S. Department of Energy. The publisher by accepting the manuscript for publication acknowledges that the United States Government retains a non-exclusive, paid-up, irrevocable, world-wide license to publish or reproduce the published form of this manuscript, or allow others to do so, for United States Government purposes.

DISCLAIMER

This report was prepared as an account of work sponsored by an agency of the United States Government. Neither the United States Government nor any agency thereof, nor any of their employees, nor any of their contractors, subcontractors, or their employees, makes any warranty, express or implied, or assumes any legal liability or responsibility for the accuracy, completeness, or any third party's use or the results of such use of any information, apparatus, product, or process disclosed, or represents that its use would not infringe privately owned rights. Reference herein to any specific commercial product, process, or service by trade name, trademark, manufacturer, or otherwise, does not necessarily constitute or imply its endorsement, recommendation, or favoring by the United States Government or any agency thereof or its contractors or subcontractors. The views and opinions of authors expressed herein do not necessarily state or reflect those of the United States Government or any agency thereof.

Noisy-Intermediate-Scale Quantum Electromagnetic Transients Program

Yifan Zhou, *Member, IEEE*, Peng Zhang, *Senior Member, IEEE* and Fei Feng, *Student Member, IEEE*

Abstract—Quantum-empowered electromagnetic transients program (QEMTP) is a promising paradigm for tackling EMTP's computational burdens. Nevertheless, no existing studies truly achieve a practical and scalable QEMTP operable on today's noisy-intermediate-scale quantum (NISQ) computers. The strong reliance on noise-free and fault-tolerant quantum devices—which appears to be decades away—hinder practical applications of current QEMTP methods. This paper devises a NISQ-QEMTP methodology which for the first time transitions the QEMTP operations from ideal, noise-free quantum simulators to real, noisy quantum computers. The main contributions lie in: (1) design of shallow-depth QEMTP quantum circuits for mitigating noises on NISQ quantum devices; (2) practical QEMTP linear solvers incorporating executable quantum state preparation and measurements for nodal voltage computations; (3) a noise-resilient QEMTP algorithm leveraging quantum resources logarithmically scaled with power system dimension; (4) a quantum shifted frequency analysis (QSFA) for accelerating QEMTP by exploiting dynamic phasor simulations with larger time steps; (5) a systematical analysis on QEMTP's performance under various noisy quantum environments. Extensive experiments systematically verify the accuracy, efficacy, universality and noise-resilience of QEMTP on both noise-free simulators and IBM real quantum computers.

Index Terms—Quantum electromagnetic transients program (QEMTP), quantum shifted frequency analysis (QSFA), quantum computing, variational quantum linear solver, noisy-intermediate-scale quantum (NISQ) era.

I. INTRODUCTION

LECTROMAGNETIC transients program (EMTP) has become a keystone of modern power system analytics. Those widely-used electromechanical dynamical simulation tools become incapable of capturing fast frequency excursions and extreme dynamics [1] in modern grids with reduced inertia. EMTP, which can accurately trace power system dynamics and generate electromagnetic waveforms of broad spectra [2], is therefore in high demand for managing today's power networks with increasingly complex operational scenarios.

Solving EMTP, however, is a long-standing obstacle [3]. The complexity of numerical integration by classical computing scales polynomially with the power system dimension, making EMTP computationally expensive even on a real-time dynamic simulator (RTDS). Recently, the swift growth in

This work was supported in part by the Department of Energy's Office of Electricity under Grant No. TE1103000-05300-3123785, in part by the National Science Foundation under Grant Nos. ECCS-2018492, OIA-2040599 and OIA-2134840.

The authors are with the Department of Electrical and Computer Engineering, Stony Brook University, Stony Brook, NY 11794-2350, USA (e-mail: p.zhang@stonybrook.edu).

quantum computing [4], [5], [6] ignites new hopes of developing unprecedently scalable EMTP analytics. In contrast to classical computing, quantum computing holds the promise of developing linear solvers with a logarithmically scaled computational complexity [6].

A prior study [7] devised an Harrow-Hassidim-Lloyd (HHL)-based quantum EMTP, which was the first attempt to integrate quantum computing with EMTP. Although the proof-of-concept was successful [7], the method's scalability on real-scale power systems and practicability on real quantum hardware remain unsatisfactory. HHL employs extremely high-depth quantum circuits even for tiny-scale problems [8], making them prone to perturbations from noisy environments [9]. In fact, the fault-tolerant quantum devices required by HHL, i.e., those with diminutive quantum errors and sufficient qubits for error correction, may not be immediately available within decades [10]. Noisy-intermediate-scale quantum (NISQ) computers are still the state-of-the-art, where the executable scale of quantum circuits is severely restricted by the limited number of qubits, low connectivity between qubits, and coherent and incoherent errors, etc [9].

The overarching goal of this paper is to enable an NISQ-device-compatible quantum EMTP (QEMTP) which allows for practical and scalable quantum EMTP simulations on the NISQ devices (e.g., quantum devices accessible at IBM Quantum Hubs). To this end, four major contributions are made as follows:

- A shallow-depth, logarithmical-width variational quantum circuit (VQC) is designed to enable reliable operations of QEMTP under noisy quantum environments.
- Practical QEMTP linear system problem (LSP) solvers are devised for the step-by-step nodal analysis. By leveraging the power network characteristics, the customized QEMTP-LSP solvers resolve the obstacles faced by the general-purpose variational quantum linear solvers (VQLSs) for quantum state preparations and measurements on real quantum hardware.
- An overall procedure of QEMTP is developed integrating the QEMTP-VQC training, the QEMTP-LSP solver, and error compensation to jointly achieve high-fidelity, noise-resilient EMTP simulations through quantum computing.
- QEMTP is further empowered with a quantum shifted-frequency-analysis (QSFA) method, which accelerates QEMTP by solving dynamic-phasor-based differential equations with larger time steps in quantum computations. A QSFA solver is established for computing the complex nodal voltage phasors at each time step.
- Systematical studies are designed to comprehensively eval-

uate the QEMTP performance under noisy quantum environments regarding both the simulation accuracy and the noise-resilience.

The remainder of the paper is organized as follows. Section II establishes the QEMTP formulation. Section III devises the NISQ QEMTP algorithm. Section IV further establishes the QSFA methodology. Section V provides extensive case studies on both quantum simulators and real IBM quantum computers to validate the proposed methods. Section VI concludes the paper.

II. QUANTUM EMTP FORMULATION

A. Classical EMTP Formulation

EMTP studies power system transients based on numerical integration rules (e.g., the trapezoidal discretization) and nodal analysis [2]. By introducing a compensated current source, each electrical component, regardless of a simple RLC component or a complex rotating machine, can be uniformly transformed into an equivalent resistance:

$$i(t) = gv(t) - i_h(t) \quad (1)$$

where $i(t)$ and $v(t)$ respectively denote the component current and voltage; g denotes the equivalent conductance and $i_h(t)$ denotes the compensated current of history states (see Table I for the detailed expressions of basic RLC components).

Table I. EMTP formulation of basis components

| Component | g | $i_h(t)$ | Graphic Illustration |
|-----------|-------------------------|-----------------------------------------------------|----------------------|
| R | $\frac{1}{R}$ | 0 | |
| L | $\frac{\Delta t}{2L} *$ | $-\frac{\Delta t}{2L}v(t-\Delta t) - i(t-\Delta t)$ | |
| C | $\frac{2C}{\Delta t}$ | $\frac{2C}{\Delta t}v(t-\Delta t) + i(t-\Delta t)$ | |

* Δt : time step.

Correspondingly, at each time step, dynamic equations of a power network can be numerically substituted by algebraic equations of an equivalent network of resistances [2]:

$$\hat{G}\hat{v}(t) = \hat{i}_s(t) + \hat{i}_h(t) := \hat{i}(t) \quad (2)$$

Here, \hat{v} denotes the vector of nodal voltages; \hat{i} denotes the vector of nodal current injections, which assembles currents from both power sources (i.e., \hat{i}_s) and history terms (i.e., \hat{i}_h); \hat{G} denotes the equivalent conductance matrix of N dimensions (i.e., number of nodes with unknown voltages).

EMTP solves (2) step-by-step to obtain $\hat{v}(t)$, and thus its essence is a Linear System Problem (LSP). Classically, solving an N -dimensional LSP leads to a computational complexity scaling polynomially in N , making EMTP intractable for large-scale systems. In contrast, quantum computing exhibits exponential speedup in tensor manipulation and is promisingly efficacious for data processing in an ultra-high-dimensional space. This motivates the establishment of an QEMTP.

B. Preliminaries of Quantum Computing

In quantum computing, a quantum state is represented by a vector in a Hilbert space. An arbitrary n -qubit quantum state can be modelled as:

$$|\phi\rangle = \sum_{k=1}^{2^n} \alpha_k |k\rangle \quad (3)$$

where $|k\rangle$ represents the k -th computational basis and $\sum_k |\alpha_k|^2 = 1$. As indicated by (3), n qubits are capable of creating a complete 2^n -dimensional vector space [11]. Therefore, any quantum operations will be of exponential dimension, as compared with classical operations.

The basic computational routine in quantum computing is a quantum circuit [12]. A variational quantum circuit (VQC) is an ordered sequence of parameterized quantum gates on quantum states. Those parameters can be optimized such that VQCs can realize various tasks (e.g., linear solver [10], eigensolver [13]).

C. Quantum EMTP Formulation

As aforementioned, $n = \lceil \log_2(N) \rceil$ qubits are required to represent an N -dimensional power system.

Reformulating the current injection i in (2) into its quantum representation gives:

$$|\mathbf{i}\rangle = \sum_{k=1}^N \frac{\hat{i}_k}{\sqrt{\sum_k \hat{i}_k^2}} |k\rangle =: \sum_{k=1}^N i_k |k\rangle \quad (4)$$

where \hat{i}_k denotes the k^{th} element of \hat{i} .

Reformulating the conductance matrix \hat{G} into a padded and normalized form gives:

$$\mathbf{G} = \begin{bmatrix} \mathcal{D}(\sqrt{\mathbf{d}_G^{-1}}) \hat{G} \mathcal{D}(\sqrt{\mathbf{d}_G^{-1}}) & \mathbf{0} \\ \mathbf{0} & \mathbf{I}^{2^n - N} \end{bmatrix} \quad (5)$$

where \mathbf{d}_G denotes a vector constructed by the diagonal elements of \hat{G} ; $\mathcal{D}(\cdot)$ constructs a diagonal matrix from the input vector; $\mathbf{I}^{2^n - N}$ denotes an identity matrix of dimension $(2^n - N)$; $\mathbf{0}$ denotes a zero matrix.

QEMTP targets at preparing a quantized nodal voltage state $|\mathbf{v}\rangle$ so that $\mathbf{G}|\mathbf{v}\rangle$ is proportional to $|\mathbf{i}\rangle$:

$$|\phi\rangle = \frac{\mathbf{G}|\mathbf{v}\rangle}{\sqrt{\langle \mathbf{v}|\mathbf{G}^T \mathbf{G}|\mathbf{v}\rangle}} = |\mathbf{i}\rangle \quad (6)$$

To achieve this goal, a variational quantum circuit (VQC) should be delicately designed for generating $|\mathbf{v}\rangle$ corresponding to \mathbf{G} and \mathbf{i} , such as:

$$|\mathbf{v}\rangle = U(\mathbf{p}) |\mathbf{0}\rangle \quad (7)$$

where U denotes a VQC parameterized by \mathbf{p} . The next section introduces how to establish such $U(\mathbf{p})$.

Equations (4)-(7) jointly form a quantum-based solution of nodal voltages. Consequently, the LSP in classical EMTP (see (2)) can be substituted by a quantum LSP (QLSP) embedded in the Hilbert space (see (7)). A salient feature of the QEMTP formulation is that the required computational resource (i.e., qubits) scales logarithmically in N , which indicates an exponential improvement over the classical EMTP.

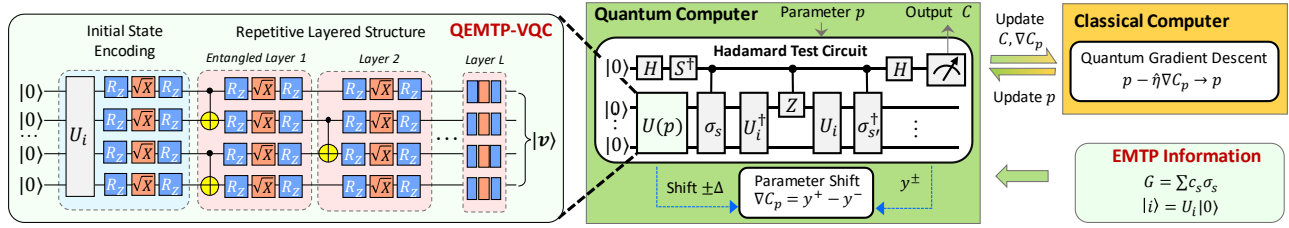


Figure 1. Schematic diagram of the VQLS-based QEMTP-LSP solver

III. VARIATIONAL QUANTUM EMTP ALGORITHM

In this section, we devise a variational QEMTP algorithm to realize the EMTP functionality in the Hilbert space.

A. VQLS-based QEMTP-LSP Solver

This subsection establishes a variational quantum linear solver (VQLS)-based QEMTP-LSP solver to prepare a proper QEMTP-VQC depicted in (7), given the conductance matrix G and nodal current injections i .

Fig. 1 illustrates the schematic diagram of the VQLS-based QEMTP-LSP solver, where a hybrid quantum-classical framework is adopted. As shown in Fig. 1, a quantum computer takes the system conductance matrix G and i as inputs, and it executes the parameterized QEMTP-VQC to obtain the quantum states of nodal voltages, i.e., $|\psi\rangle = U(\mathbf{p})|0\rangle$. Then, a classical computer updates the VQC parameters \mathbf{p} , which prompt $G|\psi\rangle$ to move towards i . The two subroutines interact to optimize the VQC's parameters until (6) is achieved. The following details the methodology.

1) *Conductance Matrix Decomposition*: First, the conductance matrix G is decomposed into a linear combination of multi-qubit Pauli operators so that its information can be represented in the Hilbert space [14]:

$$G = \sum_{s=1}^{4^n} c_s \sigma_s = \sum_{s=1}^{4^n} \frac{1}{2^n} \text{Tr}(\sigma_s G) \left(\bigotimes_{k=1}^n \sigma_{s,k} \right) \quad (8)$$

Here, $\sigma_s = \bigotimes_{k=1}^n \sigma_{s,k}$ is the s -th unitary operator; $c_s = \frac{1}{2^n} \text{Tr}(\sigma_s G)$ is the s -th coefficient correspondingly; $\sigma_{s,k} \in \{\sigma_I, \sigma_x, \sigma_y, \sigma_z\}$ is a Pauli operator applied on the k -th qubit; $\sigma_I = \begin{bmatrix} 1 & 0 \\ 0 & 1 \end{bmatrix}$, $\sigma_x = \begin{bmatrix} 0 & 1 \\ 1 & 0 \end{bmatrix}$, $\sigma_y = \begin{bmatrix} 0 & -j \\ j & 0 \end{bmatrix}$ and $\sigma_z = \begin{bmatrix} 1 & 0 \\ 0 & -1 \end{bmatrix}$ respectively denote the zeroth, x -, y - and z -Pauli matrices.

Additionally, $|i\rangle$ is also prepared by quantum operators as:

$$|i\rangle = U_i |0\rangle \quad (9)$$

where U_i is supposed to be a short-depth quantum circuit. Subsection III-B further discusses the realization of (9).

2) *Cost Function Construction*: Then, a cost function is constructed to depict the similarity between $|\phi\rangle$ (i.e., the normalized state of $G|\psi\rangle$, see (6)) and $|i\rangle$ (i.e., the normalized state of nodal current injections, see (4)). Denote $|\psi\rangle = G|\psi\rangle$, the cost function can be formulated as:

$$\mathcal{C} = 1 - |\langle i|\phi\rangle|^2 = 1 - \frac{|\langle i|\psi\rangle|^2}{\langle \psi|\psi\rangle} \quad (10)$$

Substituting (7)-(9) into (10) yields an equivalent cost function constructed by a sequence of quantum operators [10]:

$$\langle \psi|\psi\rangle = \sum_{s,s'} c_s c_{s'}^* \beta_{s,s'} \quad , \quad |\langle i|\psi\rangle|^2 = \sum_{s,s'} c_s c_{s'}^* \delta_{s,s'} \quad (11)$$

Here c_s denote the decomposition coefficients of G (see (8)); $\beta_{s,s'}$ and $\delta_{s,s'}$ are respectively modelled as [10]:

$$\beta_{s,s'} = \langle 0|U^\dagger(\mathbf{p})\sigma_{s'}^\dagger \sigma_s U(\mathbf{p})|0\rangle \quad (12)$$

$$\delta_{s,s'} = \langle 0|U^\dagger(\mathbf{p})\sigma_{s'}^\dagger U_i P U_i^\dagger \sigma_s U(\mathbf{p})|0\rangle \quad (13)$$

where $P = \frac{1}{2} + \frac{1}{2n} \sum_{j=0}^{n-1} |0_j\rangle \langle 0_j| \otimes \mathbb{1}_{\bar{j}}$. Equation (11) establishes an executable formulation of the cost function so that it can be evaluated through Hadamard test [15]. Detailed derivations of (11) and the Hadamard circuit are stated in [10].

3) *QEMTP-VQC Training*: As illustrated in (7), QEMTP optimizes a quantum circuit to obtain the nodal voltage states. The left subplot of Fig. 1 depicts the VQC designed for QEMTP, where the quantum gate arrangements are as follows:

- Initial state encoding: $|\psi_I\rangle = U_I(p_I)|0\rangle$ encoding the zero state by a RZ-SX-RZ sequence on each qubit;
- Entangled state encoding: $|\psi_E\rangle = U_E(p_E)|\psi_I\rangle$ introducing entanglement between each pair of adjacent qubits;
- Repetitive layered structure: $|\psi\rangle = U_E^{(L)} \dots U_E^{(1)} U_I |0\rangle =: U(\mathbf{p})|0\rangle$ to accomplish the QEMTP-VQC.

Then, a stochastic quantum gradient algorithm is introduced for QEMTP-VQC training, which is a quantized version of the traditional Adaptive Moment Estimation (Adam) optimizer [16]. At each iteration, the VQC parameters are updated based on the quantum gradient values:

$$\mathbf{p}_s = \mathbf{p}_{s-1} - \eta \nabla \mathcal{C}_p \quad (14)$$

Here, η denotes the adaptive learning rate; $\nabla \mathcal{C}_p$ is the quantum gradient of \mathcal{C} w.r.t \mathbf{p} calculated by parameter-shift rules [17], [18]. Upon the convergence of \mathcal{C} towards 0, optimized VQC parameters are obtained, i.e., denoted by \mathbf{p}^* .

Consequently, the optimized QEMTP-VQC circuit outputs a normalized state of the power system nodal voltages:

$$|\psi\rangle = U(\mathbf{p}^*)|0\rangle = \sum_{k=1}^{2^n} v_k |k\rangle \quad (15)$$

where v_k is the k -th element of the normalized voltage vector.

4) *Remarks*: Here, we explain the reason for designing a variational RZ-SX-RZ sequence in Fig. 1. Although any quantum operators can be utilized in the theoretical design of a quantum circuit, they may not be available on real quantum computers. Most state-of-the-art IBM quantum computers only provide 5 basis gates, i.e., CX, ID, RZ, X and SX gates (see Appendix A for detailed representations of commonly-used quantum gates). Therefore, any non-basis quantum gates will be transpiled to basis gates when executed on an IBM quantum computer. Specifically, the transpilation of RX gates and RY gates (i.e., the widely used parameterized gates in quantum

computing) involves the RZ-SX-RZ sequence, as shown in Fig. 2. Therefore, we utilize the RZ-SX-RZ ansatz in the QEMTP-VQC circuit.

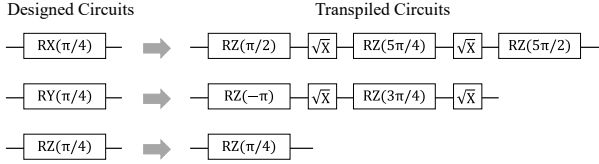


Figure 2. Transpilation of RX, RY, RZ gates on real IBM quantum hardware

Another configurable setting of the QEMTP-VQC is the number of layers. In this paper, the layer number is set by experimentation. Starting from $L = 1$, we optimize the corresponding QEMTP-VQC. If the 1-layer VQC converges to a satisfactory precision, the algorithm stops; otherwise, the layer number is increased. A larger number of layers leads to higher expressibility of the QEMTP-VQC because there will be more parameterized quantum gates that can be optimized. However, it will unavoidably deteriorate the noise-resilience of QEMTP because higher-depth quantum circuits are more sensitive to the noisy quantum environments when executed on real quantum computers.

B. Practical QEMTP-LSP Solvers

Even though the VQLS-based QEMTP-LSP algorithm can theoretically obtain the quantized nodal voltage states, its real-world application is hindered by two significant challenges.

First, a quantum state is not observable from a quantum circuit, meaning that v_k in (15) is actually inaccessible on real quantum hardware. Instead, only $|v_k|^2$ can be acquired through measurements, reflecting the possibility of the k -th basis state. In other words, even though the QEMTP-VQC prepares $|\psi\rangle$ in a Hilbert space, it does not explicitly lead to an EMTP solution \mathbf{v} in a Euclidean space.

Second, preparing an arbitrary quantum state can be computationally expensive and may lead to a high-depth circuit. For example, Fig. 3 exemplifies the quantum circuits for preparing randomly-generated $|i\rangle$. It can be seen that high-depth quantum circuits are required even for low-dimensional vectors. This indicates that (9) is possibly unrealizable in practice, considering the time-varying nodal current injections in an EMTP calculation.

Motivated by the discussion above, this subsection develops practical QEMTP-LSP solvers to conquer the state preparation/measurement barriers.

1) *Basis QEMTP-LSP Solver*: First, a basis QEMTP-LSP solver is devised. The fundamental idea is to solve a series of “basis” nodal voltage vectors corresponding to every “basis” current injection:

$$\mathbf{G} |\mathbf{v}^{(k)}\rangle = |\mathbf{i}^{(k)}\rangle, \quad |\mathbf{i}^{(k)}\rangle = |k\rangle, \quad \forall k \quad (16)$$

where $|\mathbf{v}^{(k)}\rangle$ and $|\mathbf{i}^{(k)}\rangle$ respectively denote the k -th basis voltage and current states.

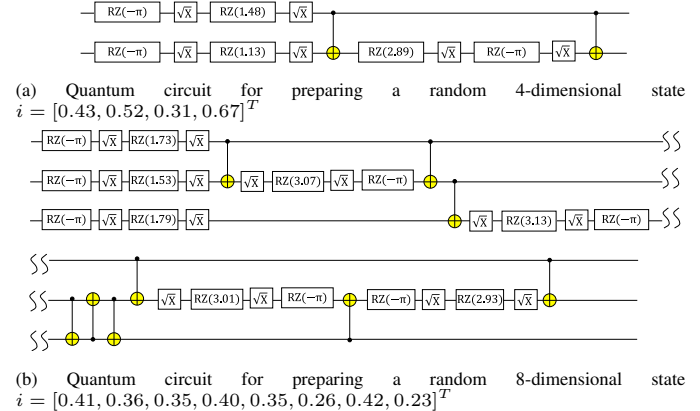


Figure 3. Exemplification of quantum circuits for preparing $|i\rangle$

| | Current State Preparation Circuit | Decomposed Conductance Matrix Circuit |
|--------------|-------------------------------------------------------------------------------------------------------------|--------------------------------------------------------------------------------|
| Basis Solver | $ i\rangle = 0\rangle \quad i\rangle = 1\rangle \quad i\rangle = 2\rangle \quad i\rangle = 3\rangle$ | $G = \sigma_{x1}\sigma_{x2} + \sigma_{y1}\sigma_{y2} + \sigma_{z1}\sigma_{z2}$ |
| | $ 0\rangle \quad 0\rangle - X \quad 0\rangle \quad 0\rangle - X$ | $X \quad Y \quad Z$ $X \quad Y \quad Z$ |
| Batch Solver | $ 0\rangle - H \quad 0\rangle - H \quad 0\rangle - H \quad 0\rangle - H$ | $\text{---} \quad \text{---} \quad \text{---}$ |
| | $ 0\rangle \quad 0\rangle \quad 0\rangle \quad 0\rangle$ | $X \quad Y \quad Z$ $X \quad Y \quad Z$ |

Figure 4. Quantum circuits for current state preparation and conductance matrix decomposition in practical QEMTP-LSP solvers. Exemplified on a 4-dimensional example, which requires 2 qubits for the basis solver and 4 qubits for the batch solver.

Proposition 1. Denote $|\mathbf{v}^{(k)}\rangle = [v_1^{(k)}, v_2^{(k)}, \dots, v_{2^n}^{(k)}]^T$. Then, $v_j^{(k)} \in \mathbb{R}$ and $v_j^{(k)} \geq 0 (\forall j)$.

Proof. See Appendix B-A. \square

Accordingly, the voltage state corresponding to an arbitrary current state $|\mathbf{i}^\circ\rangle = \sum_k i_k |k\rangle$ can be constructed as the linear combination of the “basis” voltages:

$$\mathbf{v}^\circ = \sum_k i_k \mathbf{v}^{(k)} \quad (17)$$

where $\mathbf{v}^{(k)}$ is measured from $|\mathbf{v}^{(k)}\rangle$.

This basis QEMTP-LSP solver resolves the aforementioned challenges because:

- Equation (16) only requires preparing each basis quantum state, i.e., $|k\rangle = U_i^{(k)} |0\rangle$. This can be readily achieved by applying Pauli-X gates on appropriate qubits so that $U_i^{(k)}$ is fortunately a one-depth quantum circuit. Fig. 4 demonstrates $U_i^{(k)}$ on a 4-dimensional example.
- According to **Proposition 1**, coefficients of $|\mathbf{v}^{(k)}\rangle$ are all real, non-negative numbers. Therefore, $\mathbf{v}^{(k)}$ can be straightforwardly measured from a quantum circuit as:

$$\mathbf{v}^{(k)} = [\sqrt{|\alpha_1|^2}, \sqrt{|\alpha_2|^2}, \dots, \sqrt{|\alpha_{2^n}|^2}] \quad (18)$$

where $|\alpha_s|^2$ denotes the possibility of $|\mathbf{v}^{(k)}\rangle$ on the s -th computational basis.

- 2) *Batch QEMTP-LSP Solver*: The basis QEMTP-LSP solver requires solving N QLSPs for all computational bases, as formulated in (16). A natural idea is to explore whether those

QLSPs can be solved simultaneously, exploiting the advantage of superpositions in quantum computing.

A batch QEMTP-LSP solver is therefore devised. Rather than solving each basis QLSP independently, the batch QEMTP-LSP solver gathers (16) for each k to build up an augmented QEMTP model:

$$\begin{bmatrix} \mathbf{G} & \mathbf{0} & \cdots & \mathbf{0} \\ \mathbf{0} & \mathbf{G} & \cdots & \mathbf{0} \\ \vdots & \vdots & \ddots & \vdots \\ \mathbf{0} & \mathbf{0} & \cdots & \mathbf{G} \end{bmatrix} \begin{bmatrix} \mathbf{v}^{(1)} \\ \mathbf{v}^{(2)} \\ \vdots \\ \mathbf{v}^{(2^n)} \end{bmatrix} = \frac{1}{2^{n-1}} \begin{bmatrix} \mathbf{i}^{(1)} \\ \mathbf{i}^{(2)} \\ \vdots \\ \mathbf{i}^{(2^n)} \end{bmatrix} \quad (19)$$

Equation (19) is again reformulated in its quantum representation:

$$\tilde{\mathbf{G}} |\tilde{\mathbf{v}}\rangle = |\tilde{\mathbf{i}}\rangle \quad (20)$$

where $|\tilde{\mathbf{v}}\rangle$ and $|\tilde{\mathbf{i}}\rangle$ are both $2n$ -qubit quantum states.

A notable observation is that the batch solver in the Hilbert space (see (20)) only requires an additional n qubits, whereas in the Euclidean space, it leads to an LSP scaled by 2^n times. This again demonstrates the logarithmic reduction of computational resources through quantum computing.

The following explains how the batch QEMTP-LSP solver tackles the challenges in measurements and state preparation. First, $\tilde{\mathbf{G}}$ is a block-diagonal matrix with each block inheriting the structure of \mathbf{G} , which therefore leads to a measurable quantum state $|\tilde{\mathbf{v}}\rangle$ by analogy with (18). Second, preparing $|\tilde{\mathbf{i}}\rangle$ happens to be trivial since each $|\mathbf{i}^{(k)}\rangle$ is a computational basis. Fig. 4 illustrates the general structure of the state preparation circuit, where n Hadamard gates on the first n qubits followed by a sequence of n CNOT gates readily generates $|\tilde{\mathbf{i}}\rangle$.

Moreover, the Pauli-decomposition of $\tilde{\mathbf{G}}$, which is a preparation step for VQLS as depicted in (8), can be effortlessly constructed based on the decomposition of \mathbf{G} :

$$\tilde{\mathbf{G}} = \sum_{s=1}^{4^n} c_s \left(\bigotimes_{k=n+1}^{2n} \sigma_{s,k} \right) \quad (21)$$

where c_s and $\sigma_{s,k}$ refers to the decomposition of \mathbf{G} in (8). See the derivation of (21) in Appendix B-B. The only difference between (21) and (8) is that $\tilde{\mathbf{G}}$ implements those Pauli operators on the last n qubits (see Fig. 4 for the visualized illustration). Equation (21) indicates that even though the dimension of the augmented EMTP matrix $\tilde{\mathbf{G}}$ is 2^n times larger than that of the original EMTP matrix \mathbf{G} , no additional effort is required in decomposing the conductance matrix.

C. Error Compensation

Up to this point, we have established practical QEMTP-LSP solvers to tackle the step-by-step nodal voltage computation. However, today's quantum devices are still in the noisy intermediate-scale quantum (NISQ) era. Gate errors and short decoherence time [19] inevitably disturb the quantum devices, obstructing a quantum circuit's output from being its theoretical value. Therefore, although the QEMTP-VQC trained from Subsections III-A and III-B can prepare an accurate nodal voltage state in theory, it usually fails to perfectly replicate the exact results on a noisy quantum computer.

This subsection develops an error compensation technique to ensure the accuracy of the step-by-step QEMTP under noisy quantum environments. Denote $\mathbf{R} = [v^{(1)}, \dots, v^{(2^n)}]$ as the basis voltage states estimated from a quantum computer. We reason that \mathbf{R} provides a good approximation of \mathbf{G}^{-1} according to the philosophy of VQLS. Thereby, \mathbf{G} is decomposed as $\mathbf{G} = \mathbf{R}^{-1} + \Delta\mathbf{G}$, where $\Delta\mathbf{G}$ denotes a small error term. Consequently, the following iterative process is introduced to acquire an authentic nodal voltage solution:

$$\mathbf{v}_{(s+1)} = \mathbf{v}_{(s)} + \epsilon \mathbf{R} \mathbf{r}_{(s)} , \quad \mathbf{r}_{(s+1)} = \mathbf{i} - \mathbf{G} \mathbf{v}_{(s+1)} \quad (22)$$

where $\mathbf{v}_{(s)}$ is the value of \mathbf{v} at the s -th iteration (i.e., $\mathbf{v}_{(0)} = \mathbf{v}^\circ$ as defined in (17)); $\mathbf{r}_{(s)}$ denotes the residual (i.e., $\mathbf{r}_{(0)} = \mathbf{i} - \mathbf{G} \mathbf{v}_{(0)}$); ϵ denotes the stepsize. Iterations in (22) is recursively executed until a satisfactory precision is reached. Convergence of the above iterative method is guaranteed by the following proposition.

Proposition 2. *The iterative method in (22) converges to the correct result with a proper setting of ϵ satisfying the spectral radius $\rho(\mathbf{I} - \epsilon \mathbf{R} \mathbf{G}) < 1$.*

Proof. See Appendix B-C. \square

D. Overall Procedure of QEMTP Algorithm

In summary, **Algorithm 1** presents the QEMTP procedure. When the power network configuration changes, \mathbf{G} is updated and a corresponding QEMTP-VQC is trained. Then at each timestep, $\mathbf{i}(t)$ is updated based on the previous system states to solve the unknown nodal voltages while the error compensation technique ensures the high fidelity of QEMTP results.

IV. QSFA: AN SFA-BASED QEMTP

QEMTP inherits a deficiency of classical EMTP that small discretization steps are required to trace the instantaneous values of all desirable frequency components [20]. To resolve this issue, this section empowers QEMTP with a quantum SFA (QSFA) methodology.

A. Classical SFA Formulation

SFA-based EMTP [20], [21], [22] embeds dynamic phasors into EMTP models to obtain the time-varying phasors in power grids. A salient feature of SFA is the ability to accurately calculate the envelopes of electromagnetic transients with a large time step. Moreover, the dynamic phasor results can be readily transformed back to instantaneous solutions that still accurately capture the electromagnetic transients.

Denote $\mathcal{V}(t)$ as the dynamic phasor of $\mathbf{v}(t)$ (here, the calligraphic font is used to denote complex variables). Mathematically, $\mathcal{V}(t)$ is formulated as:

$$\mathcal{V}(t) = z(t)e^{-j\omega_s t} \iff \mathbf{v}(t) = \text{Re}(\mathcal{V}(t)e^{j\omega_s t}) \quad (23)$$

where ω_s is the fundamental frequency (i.e., 60 Hz); $z(t) = \mathbf{v}(t) + jH(\mathbf{v}(t))$ and $H(\cdot)$ denotes the Hilbert transform. $\mathcal{V}(t)$ therefore provides a complex envelope of $\mathbf{v}(t)$.

Algorithm 1: Quantum EMTP Algorithm

```

1 ▷ Initialization:  $t_{emtp}$ ,  $\xi_{max}$ , system parameters;
2 for  $t \in t_{emtp}$  do
3   if Network configuration changes or Initialization then
4     Update  $\tilde{\mathbf{G}}$  and construct  $\mathbf{G}$ ;
5     ▷ QEMTP-VQC Training:
6     Decompose  $\mathbf{G}$  by (8) and prepare  $\mathbf{U}_i$  by (9) ;
7     Build QEMTP-VQC by Fig. 1 ;
8     Randomly initialize VQC parameters  $\mathbf{p}$ ;
9     Train QEMTP-VQC by Fig. 14 ;
10
11    ▷ QEMTP-LSP Solver:
12    Initialize  $\mathbf{v}_{(0)} = 0$ ,  $\mathbf{r}_{(0)} = \mathbf{i}$ ;
13    if basis solver then
14      for  $k=1:N$  do
15        Execute the QEMTP-VQC with  $|\mathbf{i}\rangle^{(k)}$  by
16        (16);
17        Measure  $\mathbf{v}^{(k)}$  by (18);
18      end
19    else
20      Construct  $\tilde{\mathbf{G}}$  and  $\tilde{\mathbf{i}}$  by (21) and Fig. III-B ;
21      Execute the QEMTP-VQC with  $|\tilde{\mathbf{i}}\rangle$  by (20);
22      Measure  $\tilde{\mathbf{v}}$  ;
23    end
24
25    Update  $\mathbf{i}(t) = \mathbf{i}_h(t) + \mathbf{i}_s(t)$ , Prepare  $|\mathbf{i}\rangle$  by (4);
26    Construct  $\mathbf{v}$  by (17);
27    ▷ Error Compensation:
28    Initialize  $\mathbf{v}_{(0)} = 0$ ,  $\mathbf{r}_{(0)} = \mathbf{i}$ ,  $s = 0$ ;
29    while  $\max|\mathbf{r}_{(s+1)}| < \xi_{max}$  do
30      | Update  $\mathbf{v}_{(s+1)}$  and  $\mathbf{r}_{(s+1)}$  by (22),  $s = s + 1$ ;
31    end
32
33    Rescale  $\mathbf{v}_{(s)}$  to  $\hat{\mathbf{v}}$  according to (2);
34    Update nodal voltage array  $\mathbf{v}_{emtp} = \{\mathbf{v}_{emtp}, \hat{\mathbf{v}}\}$  ;
35 end
36 ▷ Output: time-series QEMTP results  $\mathbf{v}_{emtp}$  ;

```

Under the dynamic phasor formulation, the SFA-based nodal equations of the power system is reformulated as:

$$\mathcal{G}\mathcal{V}(t) = \mathcal{I}_s(t) + \mathcal{I}_h(t) := \mathcal{I}(t) \quad (24)$$

Here, \mathcal{I}_s , \mathcal{I}_h and \mathcal{I} are respectively the dynamic phasors of \mathbf{i}_s , \mathbf{i}_h and \mathbf{i} in (2); \mathcal{G} is the equivalent admittance matrix.

Consequently, the major computational burden of SFA is to solve a complex LSP (24) at each time step.

B. QSFA Methodology

QSFA acquires the solution of (24) through quantum computing. Denote $\mathcal{G} = \mathbf{G}_r + j\mathbf{G}_i$, $\mathcal{V} = \mathbf{V}_r + j\mathbf{V}_i$ and $\mathcal{I} = \mathbf{I}_r + j\mathbf{I}_i$. Equation (24) is reformulated into the real number field as:

$$\begin{bmatrix} \mathbf{G}_r & -\mathbf{G}_i \\ \mathbf{G}_i & \mathbf{G}_r \end{bmatrix} \begin{bmatrix} \mathbf{V}_r \\ \mathbf{V}_i \end{bmatrix} = \begin{bmatrix} \mathbf{I}_r \\ \mathbf{I}_i \end{bmatrix} \quad (25)$$

Recalling the fact that only possibilities can be observed from a real quantum computer rather than a quantum state itself, \mathbf{V}_r and \mathbf{V}_i can not be measured unless the sign of each element is known in advance. Motivated by this observation, we

decompose \mathcal{G} into its capacitive component \mathcal{G}^C and inductive component \mathcal{G}^I :

$$\mathcal{G} = \mathcal{G}^I + \mathcal{G}^C \quad (26)$$

Without loss of generality, \mathcal{G}^C is assumed as a diagonal matrix which usually formulates the coupled capacitances of branches. Then, SFA for the inductive power network is solved by a quantum linear solver by analogy with Section III:

$$\begin{bmatrix} \mathbf{G}_r^I & -\mathbf{G}_i^I \\ \mathbf{G}_i^I & \mathbf{G}_r^I \end{bmatrix} \begin{bmatrix} \mathbf{V}_r^I \\ \mathbf{V}_i^I \end{bmatrix} = \begin{bmatrix} \mathbf{I}_r \\ \mathbf{I}_i \end{bmatrix} \quad (27)$$

where \mathbf{G}_r^I and \mathbf{G}_i^I are respectively the real and imaginary part of \mathcal{G}^I . Denoting $\mathcal{V}^I = \mathbf{V}_r^I + j\mathbf{V}_i^I$ as the complex voltage vector solved from a quantum computer, we compensate \mathcal{V}^I with \mathcal{G}^C to construct the true nodal voltages of SFA. The following iterative compensation methodology is introduced, which only introduces simple algebraic operations:

$$\mathcal{V}_{(s+1)}^I = \mathcal{V}_{(s)}^I - g_{(s)} \mathcal{G}_{ss}^C \mathcal{V}_{(s),s}^I \mathcal{V}_{(s)}^I \quad (28)$$

where s denotes the s -th iteration; $g_{(s)} = \frac{1}{1+\mathcal{V}_{(s)}^I}$. Required number of iterations depend on the number of non-zero elements in \mathcal{G}^C .

Note that (27) is a 2^{n+1} -dimensional LSP and thus $n+1$ qubits are used for QSFA computation, i.e., the required quantum computational resource only increases by one qubit compared with that for QEMTP.

V. CASE STUDY

This section verifies QEMTP with extensive experiments. Test systems range from typical EMTP test circuits [23] to standard IEEE PES feeders [24]. QEMTP is implemented on both an IBM noise-free quantum simulator (*ibmq_qasm_simulator*, a 32-qubit simulator) and a real IBM quantum computer (*ibmq_sydney*, a 27-qubit, 32-quantum volume machine).

A. Verification of QEMTP on Noise-Free Quantum Simulator

This subsection thoroughly demonstrates the versatility and efficacy of QEMTP on an IBM noise-free quantum simulator *ibmq_qasm_simulator*.

1) Exemplification of the QEMTP Procedure: First of all, we exemplify the overall QEMTP procedure on a Latency circuit [23], which is a typical abstraction to study the fast-slow dynamics characteristics of power systems (see Fig. 3). The time step for QEMTP is set as $\Delta t = 0.2\mu s$. Simulation results are provided in Fig. 4.

To solve the unknown nodal voltages $[v_2; v_3; v_4]$, 2 qubits are required in QEMTP. The very first step of QEMTP is to decompose the conductance matrix of the Latency circuit:

$$\begin{aligned} \mathbf{G} = & \sigma_I - 0.0495\sigma_{x,2} - 0.0049\sigma_{x,1}\sigma_{x,2} \\ & - 0.0049\sigma_{y,1}\sigma_{y,2} - 0.0495\sigma_{z,1}\sigma_{x,2} \end{aligned} \quad (29)$$

Next, a QEMTP-VQC with 2 qubits, 2 layers is constructed for the Latency circuit. Fig. 4(a) illustrates the training process of this QEMTP-VQC. Starting with randomly initialized parameters, VQC generates a quantum solution (see the green vector) that differs largely from the real solution (see the red

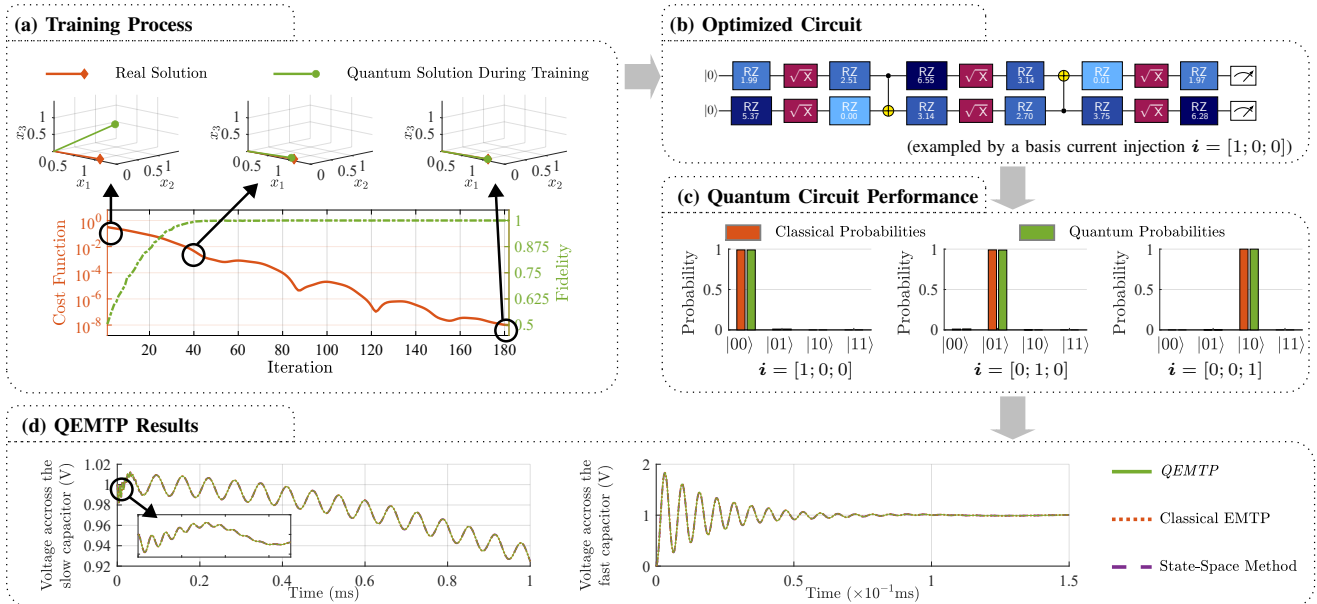


Figure 4. Demonstration of the QEMTP procedure on the Latency circuit. (a): QEMTP training procedure and the corresponding evolution of cost function and the fidelity between the real solution and the quantum solution. Vectors of the real solution and the quantum solution at typical iterations (i.e., the first, intermediate and final iterations) are also visualized. (b): Optimized quantum circuit for QEMTP (taking a basis current $i = [1; 0; 0]$ as an illustration). (c): Performance of optimized QEMTP circuits under different basis currents and the comparison with classical solutions. (d): QEMTP results and its comparison with classical EMTP results and state-space solutions.

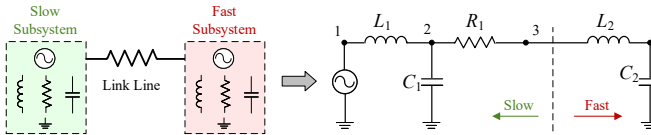


Figure 3. Illustration of the Latency circuit (see circuit parameters in [23])

vector). A large cost function and a low fidelity level can also be observed, indicating that the untrained VQC is not qualified for EMTP. Then, along the training process, the decrease of the cost function, increase of the fidelity level and approaching of the quantum solution towards the real solution jointly illustrate that the QEMTP-VQC is evolving into a well-trained quantum circuit suited for QEMTP computation.

The optimized QEMTP-VQC is depicted in Fig. 4(b). Further, Fig. 4(c) evaluates the QEMTP-LSP solver's efficacy in the Hilbert space. The perfect match between the classical and quantum probabilities of each basis state demonstrates the high fidelity of the results from the trained QEMTP-VQC.

Subsequently, Fig. 4(d) presents the QEMTP-based voltage trajectories across both the fast and slow capacitors. The QEMTP results not only accurately match the classical EMTP results and state-space solutions, but also perfectly replicate the electromagnetic transients reported in [25]. Both observations verify the correctness of QEMTP in tracing the high-frequency oscillations.

More importantly, as shown in Fig. 4(b), the QEMTP functionality is realized by a short-depth VQC with only 2 qubits, 11 depths and 2 CNOT gates. This concise quantum circuit makes it possible to truly execute QEMTP on the near-term quantum computers, meaning that the NISQ-QEMTP indeed provides a practical quantum EMTP solution (see Subsection V-B for the implementation on real quantum

hardware). This is a most salient distinction from our previous work [7]. As demonstrated in [7], our previous HHL-based QEMTP requires a 7-qubit, 102-depth quantum circuit with 54 CNOT gates for EMTP of a very simple RLC circuit, which is far beyond the quantum volume of today's quantum hardware and fails to generate meaningful results under noisy environments.

2) Demonstration of QEMTP Under Configuration Switching: Besides the normal operations, we also test QEMTP under configuration switching. Another typical EMTP test circuit, i.e., the 2-area resonant circuit [23], is employed to study the 2-area oscillation of power systems. Simulation results are presented in Fig. 5. With the switch opened at 33.33ms, the two resonant circuits become islanded.

Under configuration switching, a series of QEMTP-VQCs are trained for each configuration. As illustrated in Fig. 5(a) and Fig. 5(b), the pre-disturbance system employs a single-qubit VQC to encode the unknown voltages of the 2-area system (i.e., $[v_2; v_4]$), while the post-disturbance system employs two single-qubit VQCs to separately formulate each resonant system (i.e., v_2 and $[v_3; v_4]$). Although the electrical system's parameters remain the same, the pre-disturbance and post-disturbance VQCs are independent and do not necessarily share parameters or structures.

QEMTP results in Fig. 5(c) and Fig. 5(f) show that QEMTP maintains high fidelity to simulate the electromagnetic dynamics triggered by the switching operation, under both a poorly damped case and an improved damped case. The amplified views during the starting and switching periods specifically illustrate the perfect accuracy of QEMTP for capturing the ultra-fast transients. Again, all the QEMTP trajectories are coincident with those reported in existing studies [23], which verifies the effectiveness of QEMTP.

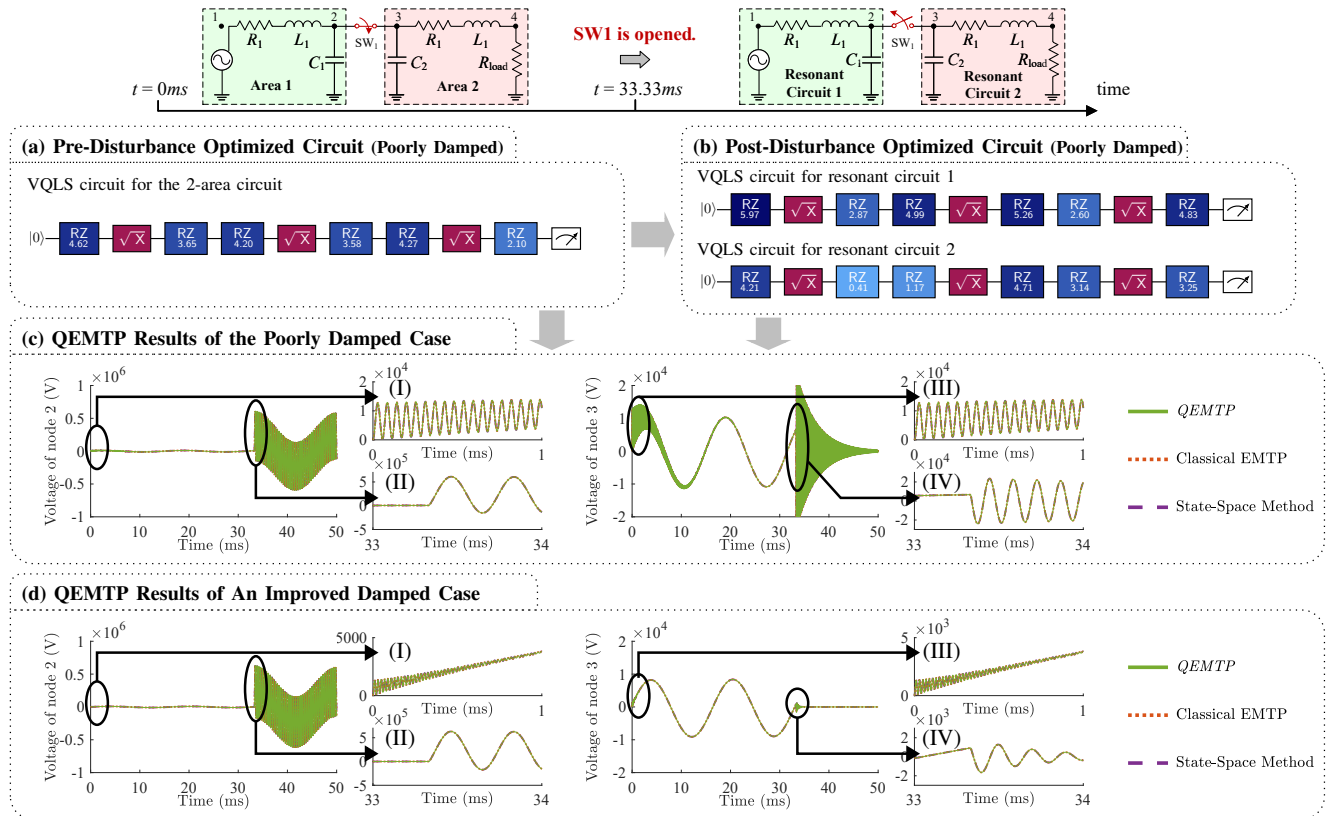


Figure 5. Demonstration of QEMTP under configuration switching. Subplots (a)-(c) investigate a poorly-damped, 2-area resonant circuit and Subplots (d) studies an improved-damped case.

3) Validity of QEMTP on Standard IEEE Test Feeders:

Further, QEMTP is verified on standard IEEE test feeders. Three test systems are studied (i.e., the 4-bus, 13-bus, 123-bus IEEE feeders [24] and the IEEE 906-bus European LV test feeder [26]) and several typical disturbances are considered (i.e., load changing, short-circuit and open-circuit) to jointly test the versatility of QEMTP. The time step for QEMTP is set as $\Delta t = 1\mu\text{s}$.

QEMTP trajectories of each test feeder are visualized in Fig. 6. It can be observed that under normal conditions, the electromagnetic transients basically exhibit a sinusoidal waveform of the fundamental frequency (i.e., 60 Hz), whereas under disturbances, high-frequency harmonics are induced. QEMTP accurately traces both the fundamental-frequency components and the irregular voltage/current distortions during the whole simulation, providing identical results with classical EMTP or state-space results.

Table II further presents a quantitative evaluation of the accuracy of QEMTP. For test systems of different scales, the QEMTP-LSP solver consistently provides high fidelity QEMTP results with an error level lower than 5×10^{-9} .

Additionally, Table II provides the comparison between quantum resources and classical resources used for EMTP. A noteworthy observation is that while the scale of the 123-bus feeder is about 10 times larger than that of the 13-bus test feeders, only 3 more qubits are required to accomplish the QEMTP computations. This again exhibits the exponential superiority of performing EMTP in the Hilbert space.

Table II. QEMTP accuracy on an IBM noise-free simulator

| | N/n^1 | VQLS Accuracy (Fidelity ²) | | QEMTP Accuracy Error (10^{-9}) | |
|----------------|---------|----------------------------------------|--------|------------------------------------|--------|
| | | Min | Mean | Max | Mean |
| Latency | 3/2 | 1.0000 | 1.0000 | 0.0131 | 0.0064 |
| 2-Area | 3/2 | 1.0000 | 1.0000 | 0.0213 | 0.0012 |
| 4-Bus Feeder | 3/2 | 1.0000 | 1.0000 | 0.8350 | 0.0672 |
| 13-Bus Feeder | 12/4 | 0.9999 | 0.9999 | 1.0051 | 0.1118 |
| 123-Bus Feeder | 122/7 | 0.9999 | 0.9999 | 2.3952 | 0.1939 |
| 906-Bus Feeder | 905/10 | 0.9999 | 0.9999 | 1.3356 | 0.4365 |

¹ N : dimension of the classical EMTP model (i.e., number of unknown nodal voltages); n : number of qubits required in QEMTP.

² Fidelity between two pure quantum states $|\psi_1\rangle = \sum \alpha_{1i} |i\rangle$ and $|\psi_2\rangle = \sum \alpha_{2i} |i\rangle$ is defined as $F(\psi_1, \psi_2) = |\langle \psi_1 | \psi_2 \rangle|^2 = (\sum \alpha_{1i}^* \alpha_{2i})^2$, which quantifies the similarity of quantum states. Here, the fidelity is computed between the quantum state obtained from QEMTP-VQC and the real solution of the linear equations, and therefore a higher fidelity indicates more accurate results.

B. QEMTP Analysis on Real, Noisy Quantum Hardware

In this subsection, we study the performance of QEMTP on a real quantum computer to verify its practicality in the Noisy Intermediate-Scale Quantum (NISQ) era [27].

1) Verification of QEMTP on the *ibmq_sydney* Quantum Computer: QEMTP is implemented on the IBM quantum computer *ibmq_sydney*, i.e., a 27-qubit, 32-quantum volume quantum computer (see Fig. 7 for its configuration and error map) and *ibmq_hanoi*, a 27-qubit, 64-quantum volume quantum

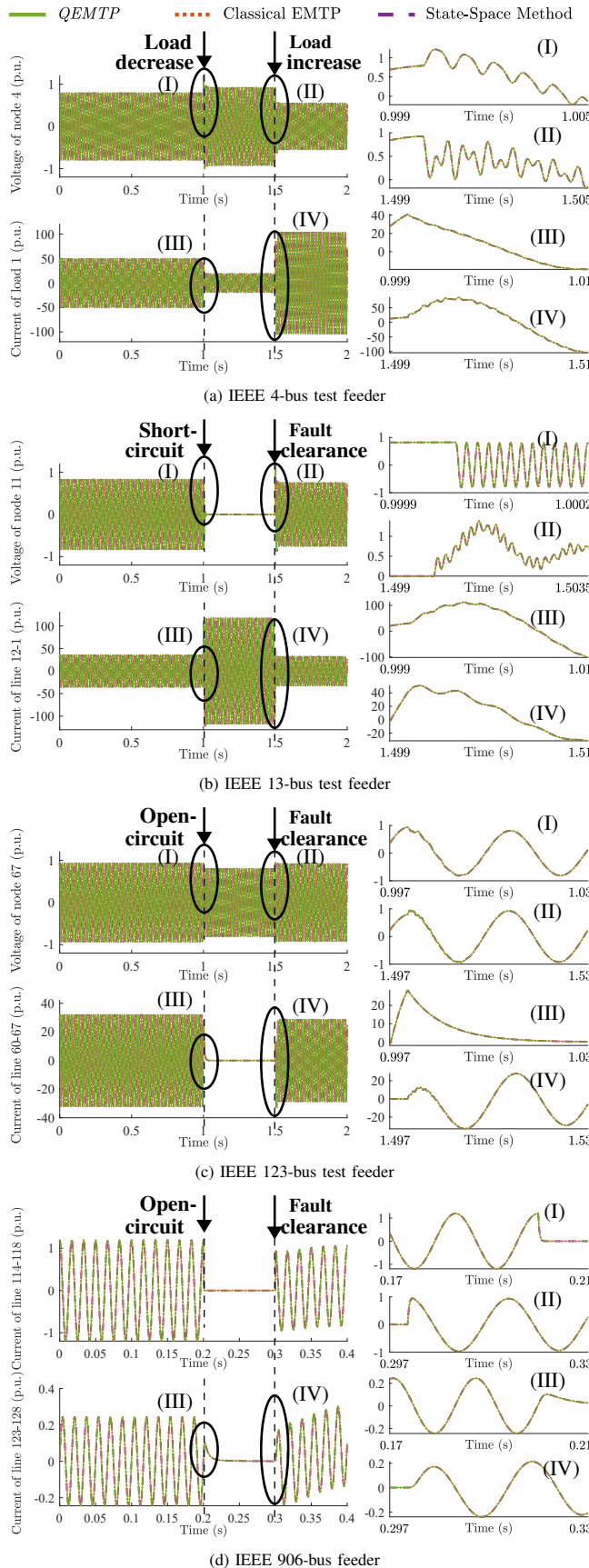


Figure 6. QEMTP results of IEEE test feeders

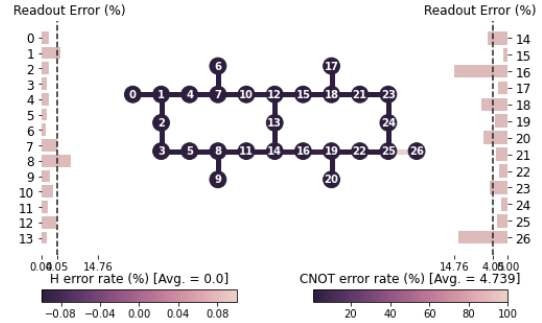


Figure 7. Configuration of the *ibmq_sydney* 27-qubit quantum computer

Table III. Comparison of QEMTP accuracy: noisy real quantum device *ibmq_sydney* vs. noise-free simulator *ibmq_gasm_simulator*

| | | Simulator (10^{-9} p.u.) | | Real machine (10^{-9} p.u.) | |
|-----------------|-------------------|-----------------------------|-------------------|--------------------------------|--------|
| | | MAE ¹ | RMSE ² | MAE | RMSE |
| Latency circuit | | 0.0064 | 0.0084 | 0.5258 | 0.6809 |
| 2-Area | Normal Fault | 0.0004 | 4.3249 | 0.0007 | 0.7102 |
| 2-Area | Normal (Improved) | 0.0012 | 1.0783 | 0.0049 | 5.055 |
| 4-Bus Feeder | Normal Fault | 0.0005 | 1.4207 | 0.0010 | 0.0068 |
| 13-Bus Feeder | Normal Fault | 0.002 | 2.7852 | 0.0009 | 0.9738 |
| 123-Bus Feeder | Normal Fault | 0.0045 | 0.0168 | 0.6531 | 0.8747 |
| 123-Bus Feeder | Normal Fault | 0.1863 | 0.2683 | 0.9567 | 1.1779 |
| 906-Bus Feeder | Normal Fault | 0.1249 | 0.1982 | 3.5906 | 4.9395 |
| 906-Bus Feeder | Normal Fault | 0.0867 | 0.1541 | 3.3037 | 5.0541 |
| 906-Bus Feeder | Normal Fault | 0.1549 | 0.2033 | 0.2584 | 0.3346 |
| 906-Bus Feeder | Normal Fault | 0.2680 | 0.3556 | 0.5021 | 0.6657 |
| 906-Bus Feeder | Normal Fault | 0.3978 | 0.5032 | 0.5627 | 0.8273 |
| 906-Bus Feeder | Normal Fault | 0.6489 | 0.8742 | 0.8816 | 0.9869 |

¹ Mean absolute error: MAE = $\text{mean}_i(y_{pi} - y_i)$ where y_{pi} and y_i respectively denote the numerical solution and the real solution.

² Root-mean-square error: RMSE = $\sqrt{\text{mean}_i(y_{pi} - y_i)^2}$.

computer³.

Fig. 8 presents the QEMTP results obtained from the real quantum computer. As a universal test, QEMTP transients triggered by different events are thoroughly studied, i.e., unsteady initial states in (a), configuration switching in (b), parametric switching in (c) and faults in (d)(e)(f). In each and every case, real-machine-based QEMTP trajectories accurately match those obtained from the quantum simulator, which evidences the effectiveness of QEMTP in simulating the electromagnetic transients on real quantum devices.

More explicitly, Fig. 9 visualizes the instantaneous error of QEMTP at each time step and Table III quantifies the QEMTP accuracy. It can be observed that QEMTP reports a slightly weakened accuracy on the real quantum computer due to the noisy environment. Meanwhile, the discrete events (such as parametric changing and faults) generally trigger a slight impulse on the errors during the step-by-step QEMTP computation. However, the overall accuracy of QEMTP under the noisy quantum environment is still high, i.e., the relative error level is consistently below 10^{-8} even for the IEEE 123-bus test feeder. This experiment indicates the robustness of QEMTP against quantum noises.

³In the following experiments, only QEMTP of the IEEE 906-bus feeder is run on *ibmq_hanoi* because *ibmq_sydney* was unavailable during the manuscript revision period.

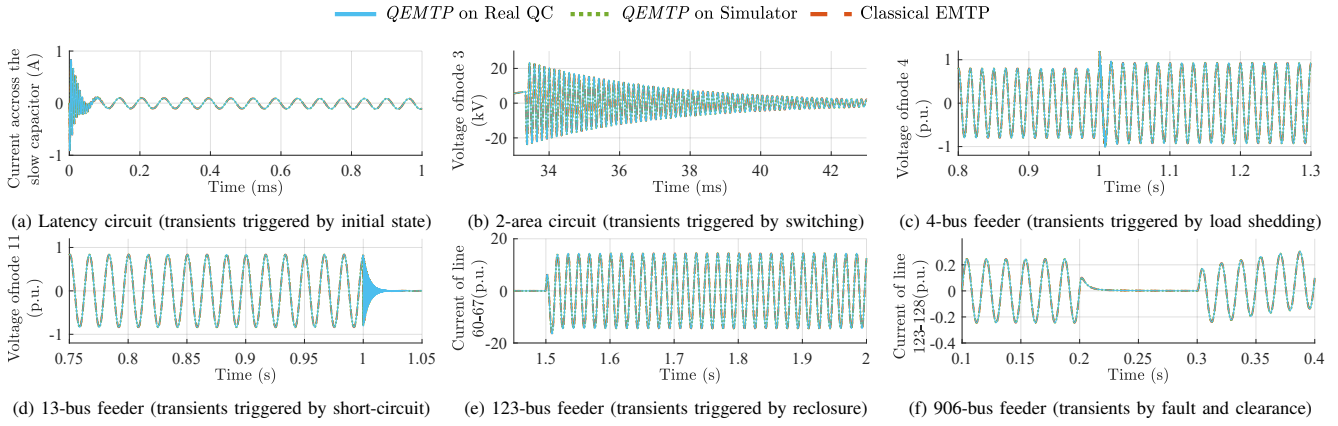


Figure 8. QEMTP results on the noisy IBM Quantum computer

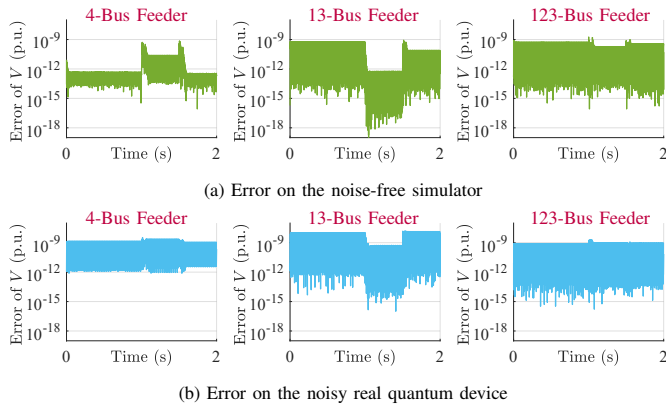


Figure 9. Step-by-step error of QEMTP: noisy real quantum device *ibmq_sydney* vs. noise-free simulator *ibmq_gasm_simulator*

Table IV. Qiskit Runtime on *ibm_hanoi* (unit: s)

| Test Case | Transpilation | Validation | Execution | Sum |
|--------------|---------------|------------|-----------|--------|
| IEEE 4-bus | 0.778 | 0.957 | 9.192 | 10.927 |
| IEEE 13-bus | 1.104 | 1.133 | 9.467 | 11.704 |
| IEEE 123-bus | 1.155 | 1.295 | 9.035 | 11.485 |
| IEEE 906-bus | 1.048 | 1.308 | 9.469 | 11.825 |

Additionally, Table IV provides the runtime of QEMTP on the IBM real quantum computer⁴, which is mainly composed of the time for transpilation, validation, and execution. Although the time consumption of QEMTP seems to be large on today's quantum hardware, a noteworthy observation is that a larger system size does not significantly increase the time consumption. As aforementioned, the reason is that QEMTP embeds the EMTP formulation from the Euclidean (classical) space into the Hilbert (quantum) space. Therefore, QEMTP can achieve exponential enhancement for tensor products over classical computing regarding the computational complexity [28].

2) *Impact of Quantum Noise:* Fig. 10 further summarizes the accuracy of QEMTP-LSP under various noisy environments. The noise model is built upon Qiskit Aer 0.8.2. [29] for simulating quantum circuits in the presence of errors.

⁴The runtime experiment is performed on *ibm_hanoi* because *ibmq_sydney* was unavailable during the manuscript revision periods.

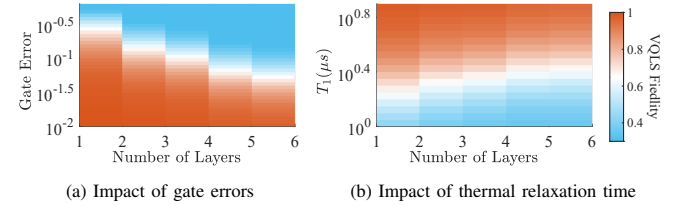


Figure 10. QEMTP performance over a range of noisy quantum environment. Subplot (a): Fidelity of the QEMTP-LSP solver over a range of gate errors. Subplot (b): Fidelity of the QEMTP-LSP solver over a range of thermal relaxation time T_1 (i.e., the time it takes for a qubit to decay from the excited state to the ground state).

Simulation shows that increasing the number of layers tends to compromise the fidelity of QEMTP-LSP, indicating that a higher-depth quantum circuit is less robust against quantum noises. On the other hand, even though deteriorated gate error and decoherence time lead to a decreased fidelity, performance of the QEMTP-LSP solver is highly assured with gate errors smaller than 0.03 or thermal relaxation time larger than 5μs. Today's quantum computers can readily achieve those noise requirements, which ensures the universal practicality of QEMTP on arbitrary near-term quantum devices.

C. Verification of QSFA

Finally, this subsection verifies the QSFA methodology, which empowers QEMTP with the SFA theory to allow for a large time step to accelerate the EMTP simulations. Without loss of generality, QSFA is demonstrated on the IEEE 4-bus test feeder. The time step for QEMTP is set as $\Delta t = 1ms$.

To solve the unknown complex voltages of buses 2-4, six variables are involved (i.e., real and imaginary parts of $[v_2; v_3; v_4]$) and therefore a 3-qubit quantum circuit is to be constructed. Equation (30) presents the decomposition of the augmented admittance matrix H of the test system for QSFA:

$$H = \sigma_I - 0.2537\sigma_{x,2}\sigma_{x,3} - 0.2537\sigma_{y,2}\sigma_{y,3} - 0.1533\sigma_{z,2}\sigma_{x,3} - 0.1274\sigma_{y,1} - 0.1533\sigma_{x,3} \quad (30)$$

The optimized QSFA-VQC for the IEEE 4-bus feeder is visualized in Fig. 11(a), which is a 3-qubit, 15-depth quantum circuit with 3 CNOT gates. Since QSFA introduces the dynamic phasor formulation, complex bus voltages are to be solved by quantum circuits, leading to a slightly more

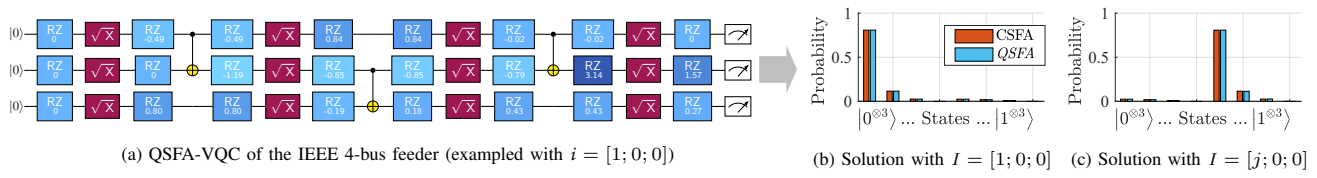
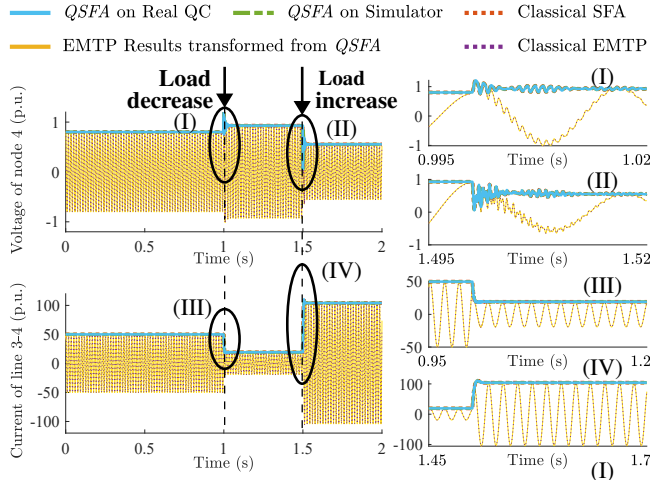
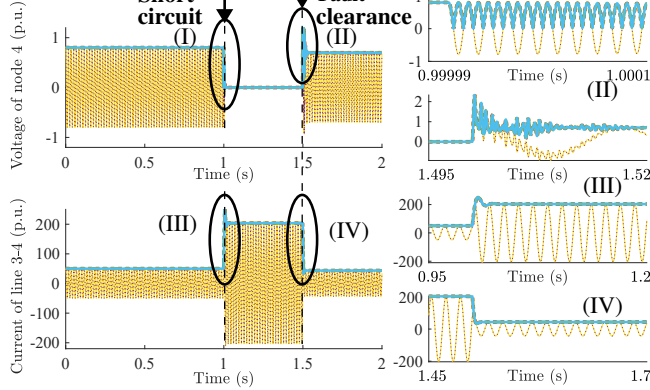


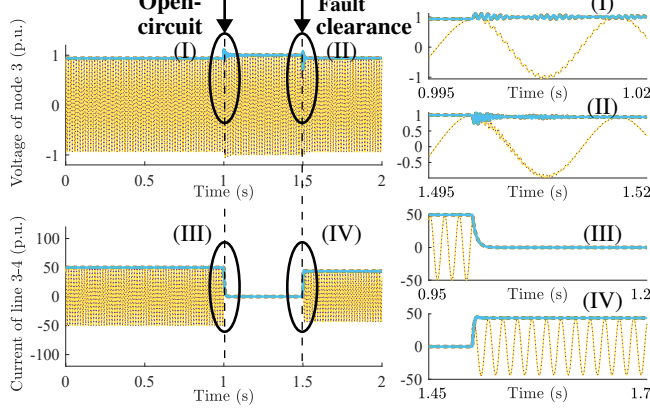
Figure 11. Quantum circuit of QSFA and the output quantum states



(a) Voltage and current transients under load fluctuation



(b) Voltage and current transients under a short-circuit fault



(c) Voltage and current transients under an open-circuit fault

Figure 12. QSFA of IEEE 4-bus test feeder under different disturbances

complicated circuit structure than that of QEMTP. Further, Figs. 11(b)(c) present the consistency between classical and

quantum probabilities under basis current injections, which verifies that the well-trained QSFA-VQC provides an efficacious solver for this complex LSP.

Subsequently, Fig. 12 provides the QSFA results under different disturbances. Several observations can be obtained:

- QSFA constructed on both the simulator and the real QC *ibmq_sydney* (see the blue and green curves) generates identical trajectories with those from the classical SFA (see the orange curves), which demonstrates the accuracy and noise-resilience of QSFA.
- QSFA offers accurate envelopes of the time-domain EMTP waveforms, which meets our expectation that the shift-frequency domain analysis can trace the system transients with a larger time step. Specifically, the dynamic phasor results indicate high-frequency oscillations on system voltages/currents after disturbances.
- Time domain results transformed back from QSFA dynamic phasors (see the yellow curves) are identical with those from the classical EMTP (see the purple curves), which also evidences the correctness of QSFA.

VI. CONCLUSION

This paper devises scalable and noise-resilient quantum EMTP analytics to allow for practical quantum electromagnetic transients analyses in the noisy-intermediate-scale quantum (NISQ) era. The devised NISQ-era QEMTP and QSFA employ shallow-depth quantum circuits and properly resolve the state preparation and measurement obstacles, and thus they truly can execute on real quantum computers and outperform our previous work [7]. QEMTP and QSFA are thoroughly validated on a real IBM quantum computer (i.e., *ibmq_sydney*) to demonstrate its accuracy, efficacy and noise-resilience. This work unlocks the potential of near-term, noisy quantum hardware for power system electromagnetic analyses.

DEDICATION

This paper is dedicated to Professor Emeritus Hermann W. Dommel on the occasion of his 89th birthday.

APPENDIX A REPRESENTATIONS OF QUANTUM GATES USED IN THE PAPER

σ_I denotes the identity gate (also denoted by I in literature), whose representation is:

$$\sigma_I = \begin{bmatrix} 1 & 0 \\ 0 & 1 \end{bmatrix}$$

σ_x , σ_y and σ_z respectively denote the Pauli X, Y, Z-gates (also denoted by X , Y and Z), whose representations are:

$$\sigma_x = \begin{bmatrix} 0 & 1 \\ 1 & 0 \end{bmatrix}, \sigma_y = \begin{bmatrix} 0 & -i \\ i & 0 \end{bmatrix}, \sigma_z = \begin{bmatrix} 1 & 0 \\ 0 & -1 \end{bmatrix}$$

\sqrt{X} (or SX) denotes the squared X gate, whose representation is:

$$\sqrt{X} = \frac{1}{2} \begin{bmatrix} 1+i & 1-i \\ 1-i & 1+i \end{bmatrix}$$

H denotes the Hadamard gate, whose representation is:

$$H = \frac{1}{2} \begin{bmatrix} 1 & 1 \\ 1 & -1 \end{bmatrix}$$

RX , RY , RZ respectively denote the single-qubit rotation gates about the X, Y and Z-axes, whose representations are:

$$\begin{aligned} RX(\theta) &= \begin{bmatrix} \cos(\theta/2) & -i\sin(\theta/2) \\ -i\sin(\theta/2) & \cos(\theta/2) \end{bmatrix} \\ RY(\theta) &= \begin{bmatrix} \cos(\theta/2) & -\sin(\theta/2) \\ \sin(\theta/2) & \cos(\theta/2) \end{bmatrix} \\ RZ(\theta) &= \begin{bmatrix} e^{-i\theta/2} & 0 \\ 0 & e^{i\theta/2} \end{bmatrix} \end{aligned}$$

CNOT (or CX) denotes the controlled Not gate, whose representation is:

$$CNOT = \begin{bmatrix} 1 & 0 & 0 & 0 \\ 0 & 1 & 0 & 0 \\ 0 & 0 & 0 & 1 \\ 0 & 0 & 1 & 0 \end{bmatrix}$$

APPENDIX B SEVERAL REMARKS FOR SECTION III

A. Proof of Proposition 1

Proof. Since $[v_1^{(k)}, v_2^{(k)}, \dots, v_{2^n}^{(k)}]^T$ is a solution of (16) and G and $|\mathbf{i}^{(k)}\rangle$ are real matrix/vector, it is obvious that $v_j^{(k)} \in \mathbb{R} (\forall j)$.

Denote $v_q^{(k)}$ as the element of the minimum value in $|\mathbf{v}^{(k)}\rangle$. Therefore, $v_q^{(k)} \leq v_j^{(k)} (\forall j)$. In the following, we prove $v_q^{(k)} \geq 0$.

Suppose $v_q^{(k)} < 0$. The current injection at node q is calculated as:

$$i_q^{(k)} = \sum_{j \in S_q} (v_q^{(k)} - v_j^{(k)}) g_j + (v_q^{(k)} - 0) g_q \quad (31)$$

where S_q denotes the set of nodes connected to node q ; g_j denotes the EMTP equivalent conductance at branch $j-q$ (see (1)); g_q denotes the equivalent conductance between node q and the ground. Based on the conductance definition, g_j and g_q are definitely positive. Therefore, (31) yields:

$$\begin{aligned} i_q^{(k)} &\leq \sum_{j \in S_q} (v_j^{(k)} - v_q^{(k)}) g_j + (v_q^{(k)} - 0) g_q \\ &< (0 - 0) g_q = 0 \end{aligned} \quad (32)$$

On the other hand, $|\mathbf{i}^{(k)}\rangle = |k\rangle$ and hence $i_q^{(k)} \geq 0$.

By obtaining a contradiction, we have proved that all the elements of $|\mathbf{v}^{(k)}\rangle$ are non-negative ($\forall k$). \square

B. Derivation of (21)

$$\begin{aligned} &\sum_{s=1}^{4^n} c_s \left(\bigotimes_{k=n+1}^{2n} \sigma_{s,k} \right) \\ &= \sum_{s=1}^{4^n} c_s \left(\bigotimes_{k=1}^n \sigma_{I,k} \bigotimes_{k=n+1}^{2n} \sigma_{s,k} \right) \quad (33) \\ &= I^{\otimes n} \left(\sum_{s=1}^{4^n} c_s \bigotimes_{k=n+1}^{2n} \sigma_{s,k} \right) \\ &= I^{\otimes n} \bigotimes G = \tilde{G} \end{aligned}$$

C. Proof of Proposition 2

Proof. Equation (22) can be reformulated as:

$$\mathbf{v}_{(s+1)} = \mathbf{v}_{(s)} + \epsilon \mathbf{R}(\mathbf{i} - \mathbf{G}\mathbf{v}_{(s)}) = (\mathbf{I} - \epsilon \mathbf{R}\mathbf{G})\mathbf{v}_{(s)} + \epsilon \mathbf{R}\mathbf{i}$$

Denote $\mathbf{A}_\epsilon = \mathbf{I} - \epsilon \mathbf{R}\mathbf{G}$ and $b = \epsilon \mathbf{R}\mathbf{i}$. Define the error at iteration s as $e_{(s)} = \mathbf{v}_{(s)} - \mathbf{v}$, where \mathbf{v} denotes the correct result of $\mathbf{G}\mathbf{v} = \mathbf{i}$. The error term therefore satisfies the following iterative step:

$$\begin{aligned} e_{(s+1)} &= \mathbf{v}_{(s+1)} - \mathbf{v} = \mathbf{A}_\epsilon \mathbf{v}_{(s)} + b - \mathbf{v} \\ &= \mathbf{A}_\epsilon(e_{(s)} + \mathbf{v}) + b - \mathbf{v} = \mathbf{A}_\epsilon e_{(s)} + (\mathbf{A}_\epsilon \mathbf{v} + b - \mathbf{v}) \\ &= \mathbf{A}_\epsilon e_{(s)} + \epsilon \mathbf{R}(-\mathbf{G}\mathbf{v} + \mathbf{i}) = \mathbf{A}_\epsilon e_{(s)} \end{aligned}$$

Correspondingly, we have:

$$e_{(s)} = \mathbf{A}_\epsilon^s e_{(0)} = \mathbf{A}_\epsilon^s (\mathbf{v}_{(0)} - \mathbf{v}) \quad (34)$$

Case 1 ($\rho(-\mathbf{R}\Delta\mathbf{G}) < 1$): Consider a special case that $\epsilon = 1$ and we have:

$$\mathbf{A}_1 = \mathbf{I} - \mathbf{R}(\mathbf{R}^{-1} + \Delta\mathbf{G}) = -\mathbf{R}\Delta\mathbf{G} \quad (35)$$

The spectral radius of \mathbf{A}_1 is defined as the maximum absolute value of its eigenvalues, i.e., $\rho(\mathbf{A}_1) = \max |\lambda|$. Since \mathbf{R} obtained from the QEMTP-LSP solvers provide a good approximation of \mathbf{G}^{-1} , $-\mathbf{R}\Delta\mathbf{G}$ is usually small compared with the identity matrix, which generally leads to $\rho(\mathbf{A}_1) < 1$. Note that $\rho(\mathbf{A}_1) < 1$ is equivalent to $\lim_{s \rightarrow \infty} \mathbf{A}_1^s e = 0$ for arbitrary vectors e . Therefore, the iteration provably converges to \mathbf{v} .

Case 2 ($\rho(-\mathbf{R}\Delta\mathbf{G}) \geq 1$): Even if $\rho(-\mathbf{R}\Delta\mathbf{G})$ is larger than 1 because of the perturbations from the noisy quantum environments, the algorithm convergence can still be guaranteed by setting a proper ϵ . Denote an arbitrary eigenvalue of \mathbf{A}_1 as λ and the corresponding eigenvector as ψ :

$$\mathbf{A}_1 \psi = -\mathbf{R}\Delta\mathbf{G}\psi = \lambda\psi \quad (36)$$

Then we have:

$$\mathbf{A}_\epsilon \psi = (\mathbf{I} - \epsilon \mathbf{R}\mathbf{G})\psi = (1 - \epsilon + \epsilon\lambda)\psi \quad (37)$$

which indicates that $\lambda_\epsilon = 1 - \epsilon + \epsilon\lambda$ is the eigenvalue of \mathbf{A}_ϵ . Correspondingly, an ϵ satisfying $|1 - \epsilon + \epsilon\lambda| < 1$ guarantees the convergence. \square

REFERENCES

- [1] T. NERC, "Odessa disturbance: Texas events: May 9, 2021 and june 26, 2021," 2021.
- [2] H. W. Dommel, *EMTP theory book*. Microtran Power System Analysis Corporation, 1996.
- [3] P. Zhang, W. Krawec, J. Liu, and P. Krstic, *ASCENT: Quantum Grid: Empowering a Resilient and Secure Power Grid through Quantum Engineering*. Proposal# 2023915, National Science Foundation, Feb. 2020.
- [4] M. A. Nielsen and I. Chuang, "Quantum computation and quantum information," 2002.
- [5] P. Kaye, R. Laflamme, M. Mosca, *et al.*, *An introduction to quantum computing*. Oxford University Press on Demand, 2007.
- [6] J. D. Hidary, *Quantum Computing: An Applied Approach*. Springer, 2019.
- [7] Y. Zhou, F. Feng, and P. Zhang, "Quantum electromagnetic transients program," *IEEE Transactions on Power Systems*, 2021.
- [8] A. W. Harrow, A. Hassidim, and S. Lloyd, "Quantum algorithm for linear systems of equations," *Physical review letters*, vol. 103, no. 15, p. 150502, 2009.
- [9] M. Cerezo, A. Arrasmith, R. Babbush, S. C. Benjamin, S. Endo, K. Fujii, J. R. McClean, K. Mitarai, X. Yuan, L. Cincio, *et al.*, "Variational quantum algorithms," *Nature Reviews Physics*, pp. 1–20, 2021.
- [10] C. Bravo-Prieto, R. LaRose, M. Cerezo, Y. Subasi, L. Cincio, and P. Coles, "Variational quantum linear solver: A hybrid algorithm for linear systems," *Bulletin of the American Physical Society*, vol. 65, 2020.
- [11] M. A. Nielsen and I. L. Chuang, *Quantum Computation and Quantum Information: 10th Anniversary Edition*. Cambridge University Press, 2010.
- [12] A. D. Corcoles, M. Takita, K. Inoue, S. Lekuch, Z. K. Minev, J. M. Chow, and J. M. Gambetta, "Exploiting dynamic quantum circuits in a quantum algorithm with superconducting qubits," *arXiv preprint arXiv:2102.01682*, 2021.
- [13] A. Kandala, A. Mezzacapo, K. Temme, M. Takita, M. Brink, J. M. Chow, and J. M. Gambetta, "Hardware-efficient variational quantum eigensolver for small molecules and quantum magnets," *Nature*, vol. 549, no. 7671, pp. 242–246, 2017.
- [14] A. R. Brown and L. Susskind, "Second law of quantum complexity," *Physical Review D*, vol. 97, no. 8, p. 086015, 2018.
- [15] D. Aharonov, V. Jones, and Z. Landau, "A polynomial quantum algorithm for approximating the jones polynomial," *Algorithmica*, vol. 55, no. 3, pp. 395–421, 2009.
- [16] D. P. Kingma and J. Ba, "Adam: A method for stochastic optimization," *arXiv preprint arXiv:1412.6980*, 2014.
- [17] K. Mitarai, M. Negoro, M. Kitagawa, and K. Fujii, "Quantum circuit learning," *Physical Review A*, vol. 98, no. 3, p. 032309, 2018.
- [18] M. Schuld, V. Bergholm, C. Gogolin, J. Izaac, and N. Killoran, "Evaluating analytic gradients on quantum hardware," *Physical Review A*, vol. 99, no. 3, p. 032331, 2019.
- [19] A. W. Cross, L. S. Bishop, S. Sheldon, P. D. Nation, and J. M. Gambetta, "Validating quantum computers using randomized model circuits," *Physical Review A*, vol. 100, no. 3, p. 032328, 2019.
- [20] P. Zhang, J. R. Martí, and H. W. Dommel, "Shifted-frequency analysis for emtp simulation of power-system dynamics," *IEEE Transactions on Circuits and Systems I: Regular Papers*, vol. 57, no. 9, pp. 2564–2574, 2010.
- [21] P. Zhang, J. R. Martí, and H. W. Dommel, "Induction machine modeling based on shifted frequency analysis," *IEEE Transactions on Power Systems*, vol. 24, no. 1, pp. 157–164, 2008.
- [22] P. Zhang, J. R. Martí, and H. W. Dommel, "Synchronous machine modeling based on shifted frequency analysis," *IEEE Transactions on Power Systems*, vol. 22, no. 3, pp. 1139–1147, 2007.
- [23] J. A. Hollman and J. R. Martí, "Step-by-step eigenvalue analysis with emtp discrete-time solutions," *IEEE Transactions on Power Systems*, vol. 25, no. 3, pp. 1220–1231, 2010.
- [24] IEEE PES AMPS DSAS Test Feeder Working Group, "IEEE Distribution Test Feeders." Available: <https://site.ieee.org/pes-testfeeders/resources/>.
- [25] F. A. Moreira and J. R. Martí, "Latency techniques for time-domain power system transients simulation," *IEEE transactions on Power Systems*, vol. 20, no. 1, pp. 246–253, 2005.
- [26] IEEE PES Distribution test feeders, "The ieee european low voltage test feeder," 03 2020.
- [27] J. Preskill, "Quantum computing in the nisq era and beyond," *Quantum*, vol. 2, p. 79, 2018.
- [28] P. Rebentrost, M. Mohseni, and S. Lloyd, "Quantum support vector machine for big data classification," *Physical review letters*, vol. 113, no. 13, p. 130503, 2014.
- [29] H. Abraham, AduOffei, and R. Agarwal, "Qiskit: An open-source framework for quantum computing," 2019.



Yifan Zhou (S'15–M'20) received the B.S. degree in electrical engineering from Tsinghua University, Beijing, China, in 2014, and the Ph.D. degree in electrical engineering from Tsinghua University, Beijing, China, in 2019. She is currently a Postdoctoral Researcher with Stony Brook University, Stony Brook, NY, USA. Her research interests include microgrid stability and control, formal methods and reachability analysis, and quantum computing.



Peng Zhang (Senior Member, IEEE) received the Ph.D. degree in electrical engineering from the University of British Columbia, Vancouver, BC, Canada, in 2009. He is a Full Professor of Electrical and Computer Engineering, and a SUNY Empire Innovation Professor at Stony Brook University, New York. He has a joint appointment at Brookhaven National Laboratory as a Staff Scientist. Previously, he was a Centennial Associate Professor and a Francis L. Castleman Associate Professor at the University of Connecticut, Storrs, CT, USA. He was a System Planning Engineer at BC Hydro and Power Authority, Canada, during 2006–2010. His research interests include AI-enabled smart grids, quantum-engineered power grids, networked microgrids, power system stability and control, cybersecurity, and formal methods and reachability analysis. Dr. Zhang is an individual member of CIGRÉ. He is an Editor for the IEEE Transactions on Power Systems, the IEEE Power and Energy Society Letters, and the IEEE Journal of Oceanic Engineering.



Fei Feng received the B.S. degree in electrical engineering from Southwest Jiaotong University, Chengdu, China, in 2016, and the M.S. degree in electrical engineering from Chongqing University, Chongqing, China, in 2019.. He is currently working towards the Ph.D. degree in electrical engineering with the department of Electrical and Computer Engineering, Stony Brook University, Stony Brook, NY, USA. His research interests include networked microgrids, power flow, state estimation and quantum computing.